Sustainable Energy & Fuels

Interdisciplinary research for the development of sustainable energy technologies

Accepted Manuscript

This article can be cited before page numbers have been issued, to do this please use: E. Campedelli, E. Squizzato, M. Rancan and C. Durante, *Sustainable Energy Fuels*, 2026, DOI: 10.1039/D6SE00452K.

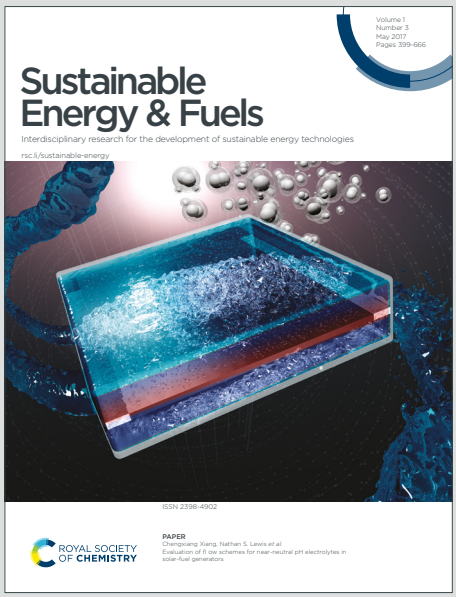

DOI: 10.1039/D6SE00452K

ARTICLE

Tracking Polarization and Passivation in Anion Exchange Membrane Electrolyzers via Current-Dependent Distribution of Relaxation Times of Electrochemical Impedance Spectroscopy

Received 00th January 20xx,
Accepted 00th January 20xx

DOI: 10.1039/x0xx00000x

Elisabetta Campedelli[a], Enrico Squizzato[b], Marzio Rancan[c], Christian Durante*[,a]

Anion exchange membrane (AEM) electrolyzers are promising for sustainable hydrogen production, however, still suffer from limited lifetime, high degradation rates, and remain a complex system to monitor. In this work, galvanostatic electrochemical impedance spectroscopy combined with distribution of relaxation times analysis enabled the deconvolution of oxygen evolution reaction, hydrogen evolution reaction, and ion transfer contributions. The break-in effect was observed and quantified, with decreasing polarization resistances in early operation. The activation of the NiFe hydroxide catalyst into NiOOH was tracked, showing improved OER kinetics within 24 h. Low-frequency features were attributed to corrosion of the nickel porous transport layer and formation of a passivation layer, confirmed by X-ray photoelectron spectroscopy. While overall performance remained stable after 48 hours at 1 A cm^{-2}, an increase in ohmic resistance was observed due to interfacial effects.

1 Introduction

Anion exchange membrane (AEM) electrolyzer represents a promising technology for the large-scale hydrogen energy storage systems. AEM technology operates on the principle of water electrolysis and enables a compact cell design, while also allowing the use of non-precious metal catalysts in a strongly alkaline environment. Moreover, AEM electrolyzers still suffer from limited lifetime and high degradation rates, and they remain complex systems to monitor. In fact, they are composed of multiple functional components, each with a distinct electrochemical role. The membrane, electrodes, catalysts, and the interfaces between components interact synergistically, determining overall efficiency, long-term stability, and optimal operating conditions. Understanding the specific contributions of each element and the dynamics of their interactions is essential for guiding the development of more efficient and economically viable electrolyzers.

Advanced measurement methods are required to optimize all components of the cell; however, further developments in operando cell monitoring are needed to achieve this goal. Half-cell potential measurements using a reference electrode are already reported in the literature and can be used to isolate the contributions of the anodic and cathodic reactions, providing insights into the origin of loss mechanisms.[1–3]

On the other hand, frequency-domain measurements, such as electrochemical impedance spectroscopy (EIS), enable the deconvolution of electrochemical processes over a wide range of frequencies, down to the mHz range. EIS is a non-destructive, in situ diagnostic tool for electrochemical cells, however, the interpretation of impedance spectra in multicomponent systems such as electrolyzers remains challenging.

The most widely used approach for EIS data analysis is the equivalent circuit model fitting, which, despite its extensive use, can be difficult to apply due to the overlap of multiple processes in such complex systems. For this reason, the distribution of relaxation times (DRT) has recently emerged as an alternative method for the analysis of EIS spectra. Although DRT analysis is widely applied in the fields of solid oxide cells and batteries, its application to AEM electrolyzers is still limited, with only a few studies reported.[3–5]

In this study, an AEM water electrolysis cell was investigated during a 48-hours degradation test in 1 M KOH electrolyte at 50 °C. The DRT analysis was employed to identify the oxygen evolution reaction (OER), hydrogen evolution reaction (HER) and ion transport polarisation processes underlying the Nyquist response. By analysing impedance spectra as a function of the applied current, the individual contributions of these processes were resolved, enabling their evolution during the break-in period to be clearly tracked. Based on these results, a stress test was performed to investigate the degradation of the cell components, revealing a passivation process occurring at the anodic porous transport layer (PTL), which is here experimentally elucidated.

2 Experimental

[a] Department of Chemical Sciences, University of Padova, via Marzolo 1, 35131, Padova, Italy.
[b] Pietro Fiorentini S.p.A., Via Enrico Fermi 8/10, 36057, Arcugnano (VI), Italy.
[c] Institute of Condensed Matter Chemistry and Technologies for Energy (ICMATE), National Council (CNR) c/o Department of Chemical Sciences, University of Padova, Via Marzolo 1, 35131, Padova, Italy.
*E-mail: christian.durante@unipd.it.

View Article Online
DOI: 10.1039/D5SE00452K

2.1 Materials

An anion exchange membrane (A60 AEM, thickness 60 μm, PiperION™) was employed. The membrane was placed between the anode and the cathode, with a total active area of 5 cm^2.

The anode electrode (NiFe, 20 mg cm^{-2}) deposited onto nickel foam using an anion exchange ionomer was provided by Pietro Fiorentini S.p.A.[6] The cathode was composed of Pt/C (0.5 mg_{Pt} cm^{-2}) deposited onto carbon cloth, using PTFE inside as binder. The described membrane electrode assembly (MEA) was sandwiched between two porous transport layers composed of a nickel mesh. The current collectors consisted of two plates, anodic and cathodic, both made of austenitic stainless steel 316L. The tubing and the reservoir for electrolyte circulation and heating were made of PTFE. A solution of 1 M KOH was prepared using demineralized water (0.9 μS cm^{-1}) and potassium hydroxide (KOH, 90%, Sigma-Aldrich) and used as electrolyte.

2.2. Experimental device and working procedure

The electrolyzer cell was provided by Pietro Fiorentini S.p.A.[6] The cell, as described in the previous paragraph, was assembled by tightening the screws to a torque of 4 Nm. The anodic compartment was then connected to a 1 L reservoir, while the cathodic compartment was connected only to the gas outlet. Specifically, in the anodic compartment, the gas-liquid mixture was discharged through a single outlet line into the reservoir, which acted as the gas-liquid separator. The reservoir and the cell were heated and controlled separately to maintain the electrolyte outlet temperature at 50 °C. The electrolyte in the reservoir was maintained at 65 °C, while the cell was placed in a chamber heated to 45–50 °C. The temperature sensor was positioned in the electrolyte outlet, as close as possible to the cell, and this location was used as the reference temperature of the system. The tests were performed at ambient pressure.

The activation procedure consisted of two steps:

1. First, the electrolyte was circulated overnight at room temperature at a flow rate of 5 mL min^{-1}.
2. Second, electrochemical activation was performed at 50 °C with a flow rate of 20 mL min^{-1}. A stepwise current ramp from 0 to 2 A (increment of 0.2 A, 9 min per step) was applied, followed by a 15 min hold at 2 A and a decrease to 0 A over 3 min. Subsequently, a linear current ramp from 0 to 2 A over 30 min was applied, followed by a 15 min hold at 2 A and a decrease to 0 A over 3 min. This final ramp was repeated once.

The electrochemical measurements and the degradation test were performed at 50°C with a flow rate of 20 mL min^{-1}.

Electrochemical activation and polarization curves were performed using Parstat 3000A-DX potentiostat. The polarization curve was recorded using current steps. Each step was reached at a current sweep rate of 10 mA s^{-1} and held constant for 200 s to allow potential stabilization. At the end of each step, a galvanostatic electrochemical impedance spectroscopy measurement was performed between 20 kHz and 100 Hz to determine the series resistance associated with ohmic losses (R_s). The R_s values were then used for the iR-correction of the polarization at each corresponding current step. Although no standardized testing protocol for AEMWE is currently established, a current density of 1 A cm^{-2} is widely adopted as a benchmark test condition, as it represents industrially relevant operation while imposing significant electrochemical stress on the cell components.[7–10] Accordingly, a current of 5 A (corresponding to 1 A cm^{-2} for the cell used in this study) was selected. The stress test was carried out using a DC power supply (HAMEG HMP4030, Rohde & Schwarz). The current was increased to 5 A in 0.25 A steps held for 1 min each, followed by a constant current of 5 A applied for a total of 48 h. Polarization curve points acquisition and EIS measurements were recorded only after complete cell relaxation to ensure reproducibility. This included stabilization of the temperature, discharge of the current collectors, and removal of gaseous products from the compartments, all of which are necessary to obtain consistent and reliable electrochemical data.

To evaluate the cell performance under prolonged operation, the stress test consisted of the initial activation procedure, followed by data acquisition before the test (0-hours test) through galvanostatic EIS (GEIS) measurements and polarization curve points. The test was then conducted under a constant current of 5 A (corresponding to 1 A cm^{-2}) for 48 h, with intermediate data acquisition after 24 h and final measurements at 48 h, each including GEIS and polarization curve recordings.

2.3 Characterization:

X-ray photoelectron spectroscopy (XPS) measurements were performed with a Thermo Scientific ESCALAB QXi spectrometer employing a monochromatic Al Kα X-ray source (1486.68 eV) operating at 200 W, a concentric hemispherical analyser, and a spot size of 900 μm × 200 μm. The pressure in the analysis chamber was better than 10^{-8} mbar. High-resolution spectra were recorded using a constant pass energy (20 eV), at 0.05 eV/step, with a dwell time of 100 ms. For further experimental details refer to.[11]

GEIS measurements were performed using a Parstat 3000A-DX potentiostat at applied currents of 0.1, 0.2, 0.5, 0.7, 1, 1.2, 1.4, and 1.6 A (corresponding to 0.02, 0.04, 0.1, 0.14, 0.2, 0.24, 0.28, 0.32 A cm^{-2}, respectively). These measurements were performed using the cell configuration by applying positive current to the anode. An AC amplitude of 10-20 % of the applied current was used, and the frequency was varied from 20 kHz to 5 mHz with 10 points per decade. Measurements were collected sequentially, with each current reached at a scan rate of 10 mA s^{-1}, followed by a 120 s stabilization period to ensure steady potentials before EIS acquisition. The EIS data were validated through the Kramers–Kronig tests discussed in details in the Supporting Information in Figure S1. The average relative error between measured and reconstructed impedance was found to be in the range of 1–2%, confirming the linearity, stability, and causality of the system within experimental uncertainty.

GEIS spectra were analysed using DRT analysis. This approach was chosen instead of equivalent circuit modelling because it

DOI: 10.1039/D6SE00452K

does not require prior assumptions about the impedance model and allows the direct extraction of characteristic time constants from EIS data, enabling the identification of different electrochemical processes, particularly in complex systems. The DRT enables the decomposition of the experimental EIS spectrum into contributions from electrochemical processes characterized by distinct relaxation times (or the corresponding frequencies). The DRT was extracted from the experimental EIS data following the approach proposed by Wan et al. and Saccoccio et al., using their open-source software DRT-tools [12,13]. DRT-tools were used with Gaussian discretization and a regularization parameter of 10^{-3}, following common practice in AEM electrolyzer studies.[4,5] Higher values of the regularization parameter produced overly smooth DRT curves, complicating interpretation, while lower values caused overfitting. The analysis of the optimization of the regularization parameter for the DRT in this study is reported in Figure S2, together with the corresponding discussion.

More in details, the DRT approach aims to reconstruct the function $\gamma(\ln f)$ from EIS data Z(f), according to:

$$Z(f) = R_s + \int_{-\infty}^{\infty} \frac{\gamma(ln\, f)}{1 + j\, f/f_c}\, d\, lnf$$

Where R_s is the ohmic resistance, f is the frequency of the EIS measurements and f_c is the characteristic frequency of the electrochemical process.

This inverse problem does not admit a unique and stable solution and is therefore treated using regularization techniques. The function $\gamma(\ln f)$ is discretized and approximated as a linear combination of radial basis functions (RBFs):

$$\gamma(ln\, f) \approx \sum_k x_k \phi_k\, (\ln f)$$

Where x_k are the coefficients to be determined and the ϕ_k are Gaussian basis functions. The coefficients are determined by fitting the experimental impedance data while enforcing smoothness through Tikhonov regularization. The resulting linear system is solved numerically to obtain the DRT over a refined frequency grid. For more information on DRT calculations, the reader is referred to the work of Saccoccio et al. and Wan et al.[12,13]

The three different approaches for handling inductance proposed by the DRT code of Ciucci were considered and discussed herein. Specifically, the fitting without inductance ignores the inductive component, assuming a pure resistive-capacitive (RC) response instead of a full RLC model (with L corresponding to the inductance); thus, the real part of the impedance at high frequencies is treated as purely resistive, neglecting R+jωL. The fitting with inductance estimates an inductive term simultaneously with the DRT. On the other hand, the fitting discarding the inductive data removes the EIS data corresponding to -Z''<0. In Figure 1 the three fittings applied to the cell system studied here are shown. In Figure 1a it is possible to observe that from approximately 30 Hz the DRT curves diverges, even though there originate from the same EIS dataset. These discrepancies are also reflected in the corresponding EIS fitting in Figure 1b, where the fittings obtained by discarding the inductive data or fitting without inductance fail to fit the EIS data in the high frequency range.

View Article Online
DOI: 10.1039/D6SE00452K

ARTICLE

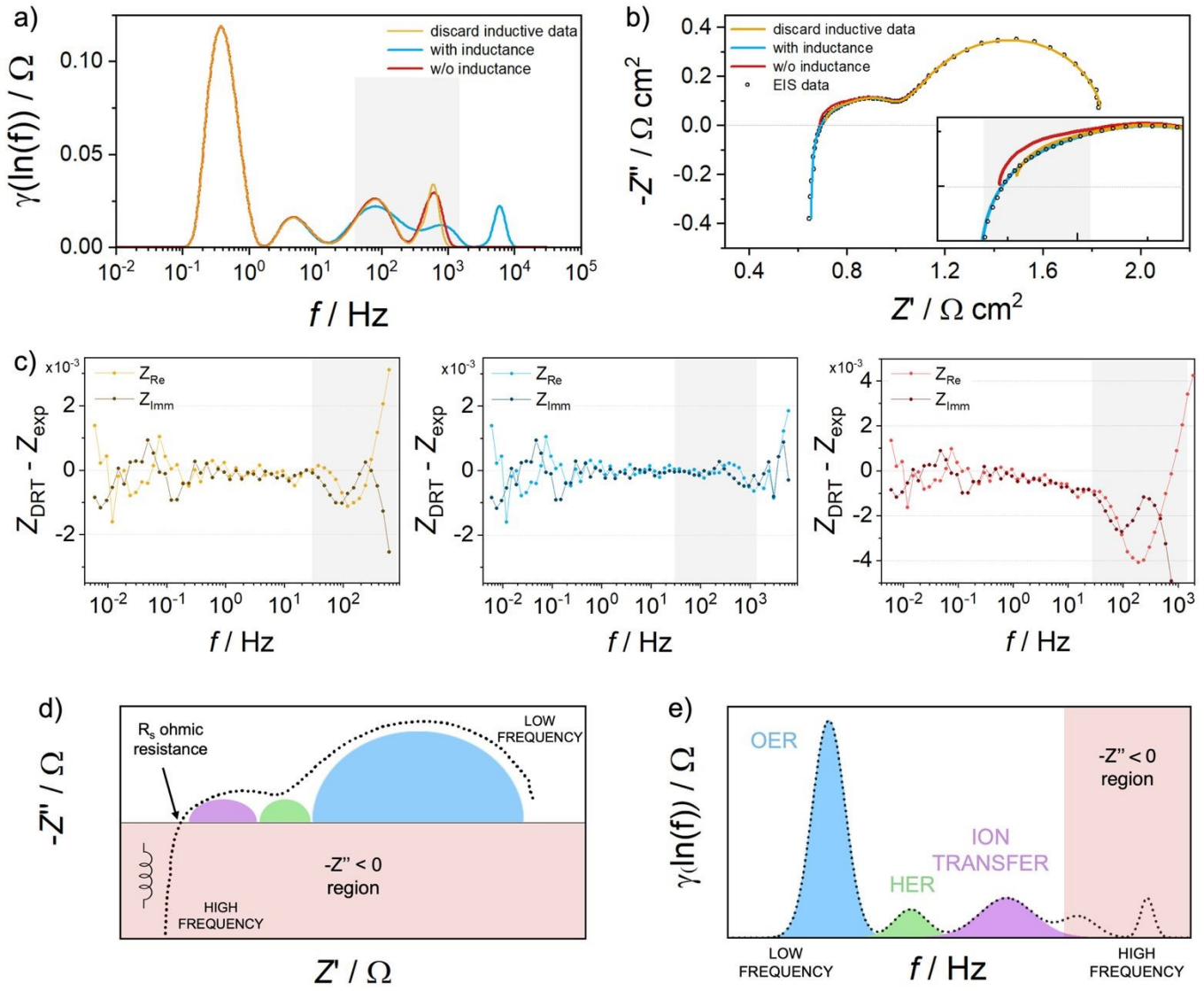

Figure 1 – a-b) DRT curves and the corresponding EIS fitting in the Nyquist plot acquired at 0.1 A, respectively. Three fitting approaches are shown: fitting discarding the inductive data, fitting with inductance and fitting without inductance. c) Residuals of the three fitting approaches: from left to right, fitting discarding the inductive data, fitting with inductance and fitting without inductance. The grey region highlights the frequency range of approximately 30-1200 Hz. d-e) Schematic illustration of experimental GEIS data (Nyquist plot) and the corresponding DRT plot. The inductive region (-Z''<0) is highlighted in red, while the polarisation processes of the AEM electrolyzer cell are shown in blue, green and violet, corresponding to OER, HER and ion transport, respectively.

This behaviour is due to the presence of a significant inductance in the system, which cannot be properly modelled by the fitting without the inductance contribution or the fitting discarding inductive data. To further investigate the fitting quality, the residuals are reported in Figure 1c, where the frequency region of interest (30-1200 Hz), affected by fitting issues, is highlighted in grey. The residuals obtained from the fitting discarding the inductive data as well as the fitting without inductance exhibit systematic trends deviating from zero; in contrast the fitting with inductance yields residuals that are randomly distributed around zero, indicating a good agreement between the model and the experimental data. For this reason, the fitting with inductance was selected for this study and two peaks appear in the frequency region with inductive behavior (-Z''<0) corresponding to high frequencies in Figure 1a. These peaks may originate from non-ideal or mathematical artifacts of the

View Article Online
DOI: 10.1039/D6SE00452K

DRT inversion, as the method is primarily suited for resistive-capacitive processes, therefore the frequency range was limited to 600 Hz after DRT calculation discarding the frequency beyond 600 Hz, as shown in Figure 1d and 1e. To better valuate the different approaches for handling the inductance contribution in DRT analysis, the effect of each choice on the quantification of the high frequency peak is provided in the Supporting Information in Figure S3 and Table S1.

Moreover, it is worth noting that the DRT curves in the region -Z''<0 (600-10000 Hz) show two peaks when inductance is included in the fitting, whereas only one peak is observed when fitting discarding inductive data o fitting without inductance is used. This behavior likely arises because, when L is included in the fitting, the DRT model separates the pure inductive contribution ($j\omega L$) from an additional contribution that is not fully captured by the model.

In the DRT plot, the characteristic frequency (f_c) of each polarization process corresponds to the position of the peak maximum in the $\gamma(\ln f)$ versus f plot as shown in Figure 1d.

The DRT curve was deconvoluted to obtain the underlying contributions shown in Figure 1d. The area under each peak was calculated by integrating $\gamma(\ln f)$ versus $\ln f$ as shown in Equation S1, yielding the resistance associated with the corresponding polarization process.

3 Results and Discussion

In the AEM water electrolyzer (AEMWE) the HER occurs in the cathodic compartment according to:

$$2H_2O + 2e^- \rightarrow H_2 + 2OH^-$$

Since in alkaline environment there are no free H^+ ions, molecular hydrogen is produced via water dissociation resulting in slower HER kinetics compared to acidic conditions. Consequently, the Volmer step (water dissociation) is required and is followed by either the Heyrovsky or the Tafel step for the hydrogen formation and release.

The OH^- ions generated during the HER migrate through the membrane to anodic compartment, where the OER takes place:

$$4OH^- \rightarrow O_2 + 2H_2O + 4e^-$$

The OER is a multistep reaction involving the transfer of four electrons and is, therefore, kinetically slower than the HER. It proceeds through the formation of surface oxide species and peroxide intermediates.

These kinetic differences are reflected in EIS measurements. In EIS, the characteristic frequency of a process is inversely related to its time constant ($f_c=1/\tau_c$), meaning that faster processes appear at higher frequencies, while slower ones are observed at lower frequencies. Accordingly, the HER is typically associated with the high-frequency region, whereas the OER appears at lower frequencies due to its slower kinetics.[4,5,14]

EIS measurements analysed using the DRT method allow the identification of the main processes occurring in the electrolyzer cell. EIS response of the cell as a function of the applied current is reported in the Nyquist plot of Figure 2a. The series of resistance associated with ohmic losses (R_S) slightly decreases with increasing current density. This behaviour is reasonable because, as the applied current increases, the dissipated power also increases, leading to a rise in cell temperature. Consequently, the ionic mobility within the membrane increases, resulting in a reduction of the membrane ohmic resistance. Even a temperature increase of 1-2 °C can cause a decrease of few $m\Omega \cdot cm^2$, according to the Arrhenius relationship that correlates ionic conductivity with temperature.

In Figure 2a, the impedance spectra exhibit two main semicircles, both decreasing in diameter as the applied current increases. However, their interpretation can be challenging because electrolyzer cells are complex systems composed of multiple components and coupled electrochemical and mass-transport processes. Since EIS analysis based on equivalent circuit modelling requires a priori knowledge of the circuit elements representing the cell, the DRT approach was selected as a more model-independent method to deconvolute the different contributions. In Figure 2b, a well-defined peak can be clearly observed at low frequencies, which can be associated with anode charge transfer, and a second peak appears at intermediate frequencies with lower intensity, corresponding to cathode charge transfer. This is consistent with the fact that the cathode is a platinum group metal (PGM) catalyst, which is expected to exhibit lower charge transfer resistance and, consequently, a smaller peak in the DRT graph.[4,5]

View Article Online
DOI: 10.1039/D6SE00452K

ARTICLE

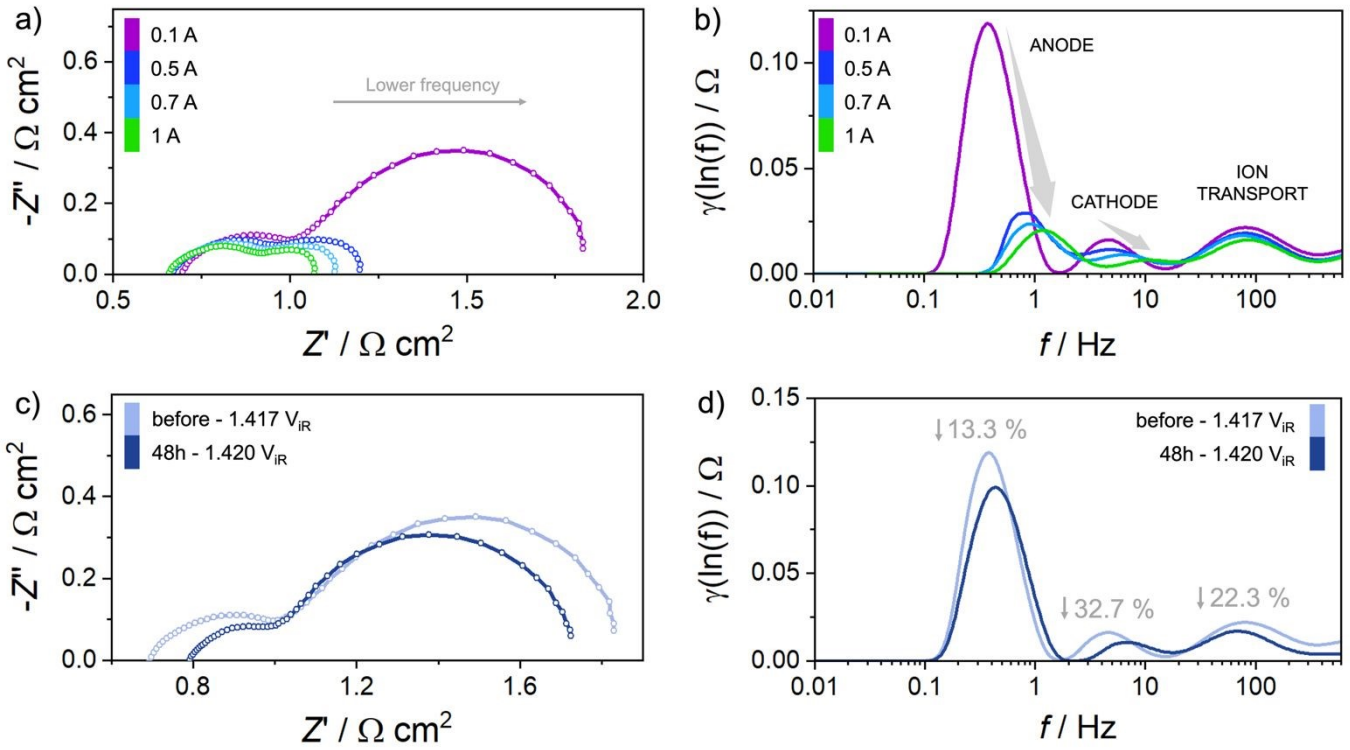

Figure 2 – a-b) Nyquist plot from GEIS data as a function of the applied current and the corresponding DRT plots. c-d) Nyquist plot from GEIS data and corresponding DRT plot before and after 48-hours stress test at the applied current of 0.1 A. The iR-corrected cell potential values are reported, as well. The percentage decrease in polarization resistance is reported for each peak, corresponding to the anodic OER, cathodic HER, and ion transport processes (from left to right, respectively).

At the cathode, the alkaline HER involves only a two-step reaction, whereas the anode OER proceeds through a four-step mechanism. Therefore, it is reasonable that the cathode charge transfer appears at higher frequencies in Figure 2b. Finally, a third peak is observed at high frequency, showing a nearly constant behaviour, which likely corresponds to contributions from ion transport within the catalyst layer.[4] The behavior of the ion transport DRT peak was investigate in more detail, and the corresponding discussion is reported in Figure S5.

Furthermore, the OER and HER peaks in Figure 2b are the only ones whose intensity decreases with increasing current, while their characteristic frequencies shift to higher values as the current increases, consistent with the acceleration of electrode kinetics under higher overpotential conditions.

After experimentally verifying the interpretation of the Nyquist plot of the electrolyzer cell used in this study, a 48-hour stress test at 5 A was applied.

The EIS comparison before and after the 48-hour stress test was performed at comparable polarization potentials to investigate the polarization processes. Although potentiostatic EIS could be used to maintain the same cell potential, variations in the R_s during operation would lead to different polarization potentials before and after the stress test. Therefore, galvanostatic EIS was preferred to ensure comparable polarization conditions despite changes in R_s, while also allowing its contribution to be monitored and distinguished from other cell processes. In Figure 2c-d, the Nyquist plots and the corresponding DRT spectra of the GEIS measurements, recorded before and after the 48-hour test, are shown together with the voltage corrected for R_s, which corresponds to the polarization voltage. In Figure 2c, the Nyquist plot after a 48-hour test shows a smaller semicircle, indicating reduced polarization resistance and changes in the electrochemical behaviour. To better understand how each polarization process has changed, the DRT curves before and after the 48-hour test are shown in Figure 2d. A reduction in polarisation resistance of 13.3%, 32.7%, and 22.3% is associated with OER, HER, and ion transport, respectively. Moreover, the OER and HER peaks shifted slightly to higher frequency after a 48-hour test, indicating an acceleration of the electrochemical processes. This behaviour is most likely due to the so-called break-in effect, during which the cell performance improves at the beginning of

operation until reaching a stable state.[8] This aspect will be discussed in more detail in the following paragraph.

On the other hand, the ion transport peak of Figure 2d shifts to a lower frequency after a 48-hour test, despite showing a decreased area. This unusual behaviour can be explained by local dehydration within the catalyst layer, which creates ion transport pathways with different rates, resulting in a broader distribution of time constants and, consequently, a peak at a lower frequency.[15]

Figures 3a–b shows the Nyquist spectra acquired at different currents at the beginning of the experiments (0-hour stress test). As expected, the semicircle diameters decrease with increasing current, as highlighted by the arrows. In addition, starting from 0.7 A, impedance points at low frequencies appear in the -Z'' < 0 region, eventually forming a dominant loop in the spectrum at 1.6 A which can be attributed to complex charge-transfer phenomena associated with localized corrosion or the formation of a passive layer of metals.[16–18]

The semicircle at lower frequencies is essentially the same for the spectra at 1.2 A and 1.4 A. The spectrum is therefore nearly identical across the entire frequency range for these currents; however, at higher frequencies the semicircle is primarily determined by ion transport, effectively masking the HER contribution and making it indistinguishable in the Nyquist plot. DRT analysis of Figure 2b enables the identification of this contribution and reveals that the ion transport is independent of the applied current, thus explaining why the high-frequency semicircle does not decrease with increasing current.

After 24 hours of testing at 5 A, the Nyquist plots as a function of applied current are shown in Figures 3c–d. Again, the semicircles follow the same trend observed in Figures 3a–b; however, the spectrum at 1.2 A exhibits scattered data points, indicating non-equilibrium electrochemical behaviour in the low frequency range. Subsequently, the low-frequency semicircle shows a significant increase in size, which becomes even larger at 1.6 A.

The instability appears only after long-term operation at 5 A followed by an overnight rest, and it is reproducible under these conditions. This suggests that it is caused by a state change in the electrode/electrolyte system induced by high current. At 5 A, the Ni surface probably undergoes strong oxidation, forming Ni oxide and hydroxide species and modifying the film structure. This makes the layer more sensitive to slow processes such as gas bubble coverage and interfacial redox dynamics, leading to loss of stability at low frequency at 1.2 A. At 1.4 A, enhanced oxygen evolution may improve NiOOH stability and accelerates bubble removal, stabilizing the interface and restoring a clear GEIS response.

After 48 hours of testing at 5 A, the spectra and their current-dependent behaviour are identical to those observed at 24 hours. This suggests that the phenomena occurring during the first 24 hours stabilized during the subsequent 24 hours, as the EIS data after 24 and 48 hours are largely the same. This correspond to the break-in effect of the cell, which is related to electrode activation and progressive stabilization of the electrode–electrolyte interfaces and is demonstrated to be confined to the first 24 hours of cell operation in this study.

More in detail, it is hypothesized that during the first 24 hours at 5 A, the NiFe catalyst undergoes surface reconstruction,

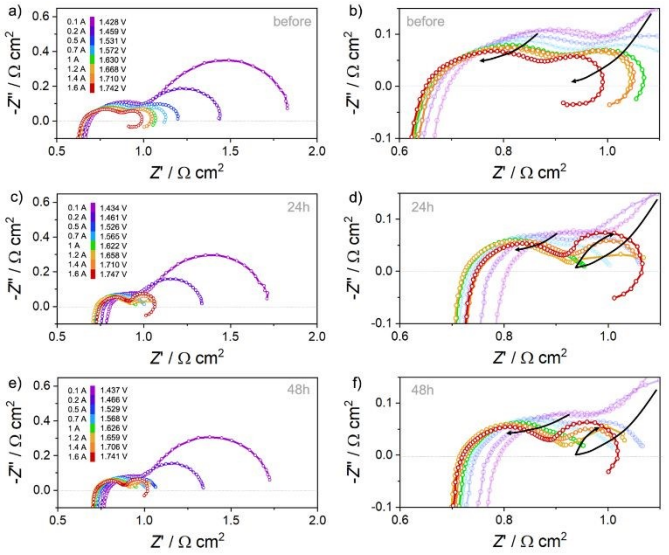

Figure 3 – Nyquist plots of galvanostatic impedance spectra as a function of applied current after 0 h (a–b), 24 h (c–d), and 48 h (e–f). Figures b, d, and f are magnified views of Figures a, c, and e. The real and imaginary components are reported as resistance multiplied by the electrode surface area, using the geometric electrode area of 5 cm². The cell voltage corresponding to each applied current is also reported.

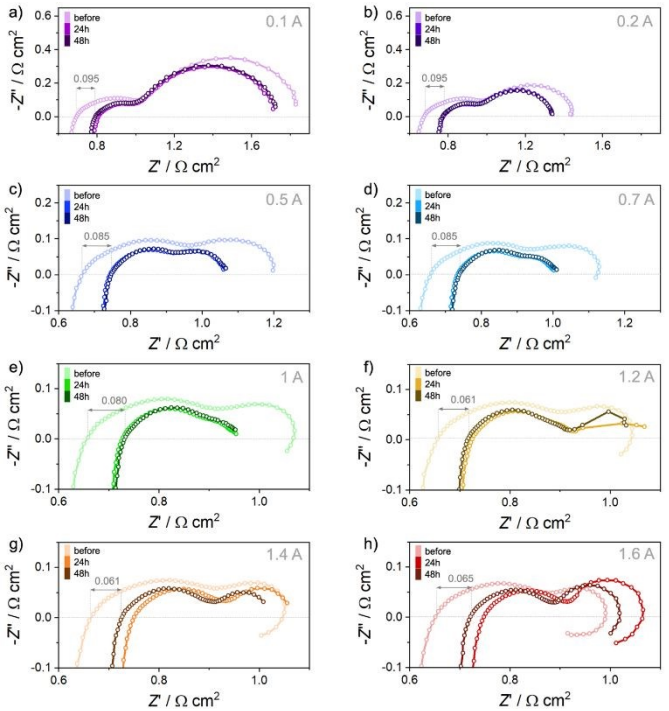

Figure 4 – Nyquist plots of galvanostatic impedance spectra before, after 24 h and 48 h for each current applied. The real and imaginary components are reported as resistance multiplied by the electrode surface area, using the geometric electrode area of 5 cm². The values reported in the graphs follow the same unit as the x-axis label.

leading to the transformation of nickel (II) hydroxide into the active NiOOH phase, Fe incorporation and/or redistribution, and a consequent increase in the electrochemically active surface area. Although a cell activation procedure was

performed before the 48 hours durability test, the anodic electrocatalyst appeared fully activated after 24 hours of operation at 5 A. This also explains the significant reduction of the low-frequency semicircle after 24 h compared to 0 h (Figure 3b and 3d) and as will be discussed in more detail in the next paragraph.

On the other hand, the inductive loop observed at 1.4 and 1.6 A in Figure 3a–b could be associated with both NiOOH formation at the anodic electrode and/or Ni degradation within the PTL in the anodic compartment. After 24 h, NiOOH formation is assumed to be completed, as previously discussed. Therefore, the anomalies appearing with a similar trend after 24 h and 48 h (Figure 3c–d and Figure 3e–f, respectively) can be attributed to the growth of a Ni passivation layer on the PTL. This interpretation is consistent with the findings of Huang et al., who reported that at pH values above ~4.9 up to pH 14, Ni surfaces undergo electrochemical passivation through the formation of NiO and $Ni(OH)_2$ layers, as predicted by DFT-based Pourbaix diagrams.[19]

Figure 4 reports the Nyquist plots for each current value. In general, the semicircle size decreases from 0 h to 24 h and then remains unchanged between 24 h and 48 h. The GEIS measurements in Figure 4 allow for a detailed analysis of the R_S values. In general, an increase in R_S is observed after 24 hours (from 0.061 to 0.095 $\Omega \cdot cm^2$); however, no further increase is detected after an additional 24 hours. This not only

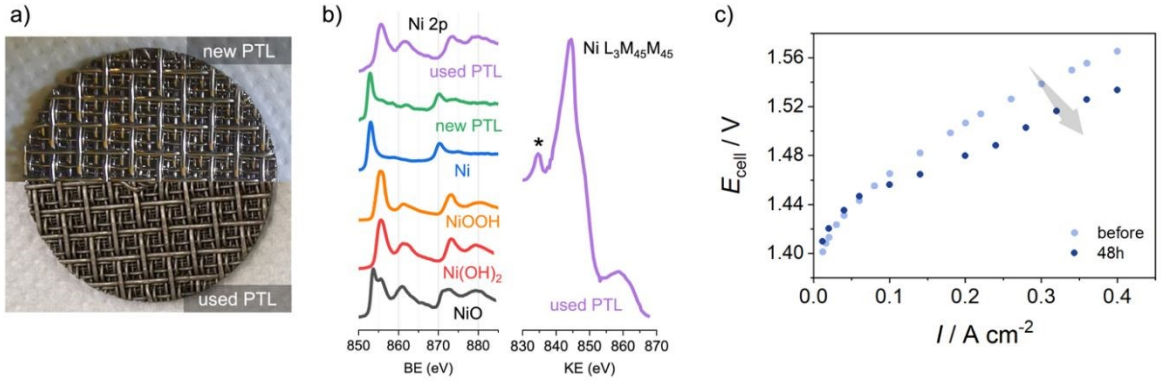

Figure 5 – a) Porous transport layer used in the anodic compartment before (new PTL) and after 48 hours (old PTL) of operation at 1 A cm^{-2}. b) Ni 2p spectra for the new PTL (green) and for the used PTL after 48h (violet), compared with reference spectra of Ni, NiOOH, $Ni(OH)_2$, NiO along with the Ni $L_3M_{45}M_{45}$ Auger peak for the used PTL.The asterisk at 833.2 eV highlights the peak characteristic of NiOOH. c) iR-corrected polarization curves of the cell before, after 24h and 48h of operation at 1 A cm^{-2}.

confirms the presence of a resistive contribution, but also further indicates that the cell after 24 hours differs from its initial state, while remaining essentially unchanged between 24 and 48 hours. Therefore, a process or structural change likely occurred during the first 24 hours of cell operation and subsequently stabilized as already discussed in relation to the break-in effect. In Figure 4f, scattered points at low frequencies are observed only after the 24-hour and 48-hour tests, without forming a well-defined semicircle. At 1.2 A, the current is insufficient to allow a single dominant mechanism to prevail, resulting in non-stationary behaviour at low frequencies. In contrast, at 1.4 A the system stabilizes, forming a coherent semicircle that terminates with a negative imaginary component, indicative of inductive processes associated with passivation/depassivation dynamics.

In Figure 4h, it is evident that the low-frequency semicircle, previously associated with corrosion processes in this study, increases after the 24-hour test and then decreases after 48 hours. In contrast, in Figure 4g, no significant difference is observed between the measurements. This behaviour is likely related to the applied current: at 1.4 A, the degradation stabilizes, while at the higher current (1.6 A), temporary dynamics of corrosion and passivation are revealed between the 24 and 48-hour tests.

The Nyquist plot of Figure 4g and 4h are the only cases in which R_S values differ between the 24h and 48h, likely due to a temperature variation, whereas R_S remained unchanged in all the other tests.

The increase of the R_s could be attributed either to the membrane degradation, as well as the formation of the passivation layer with lower conductivity compared to the original metal surface. However, PiperION™ AEM membrane was selected for this study due to its high chemical robustness and operational stability compared with other commercial membranes, as demonstrated by M. Càmaras-Miguel et al.[20] In their work, the degradation is attributed to the degradation of the piperidinium cationic groups via a Hofmann elimination mechanism under strongly alkaline conditions (ex-situ accelerated test in 1 M KOH at 80°C for 168 hours). Therefore, while the membrane degradation is in principle possible, a significant contribution within 24 h of operation using the PiperION™ AEM membrane is considered less probable, and the observed increase in R_s is more plausibly related to interfacial contact effects.

At the end of the 48-hour test, the cell was disassembled and opened. It was observed that, after cleaning with demineralized water, the PTL from the anodic side appeared opaque and slightly darker. A comparison between the new and the used PTL is shown in Figure 5a. The XPS analysis of the PTL is reported in Figure 5b along with reference spectra for the Ni 2p photoemission region of Ni, NiO, $Ni(OH)_2$ and NiOOH pure samples. The Ni 2p spectrum of the new PTL indicates that the surface is predominantly composed of metallic Ni, with a Ni $2p_{3/2}$ binding energy (BE) of 852.6 eV, with a minor contribution

DOI: 10.1039/D6SE00452K

from oxidized Ni species. In contrast, the used PTL clearly shows the absence of metallic Ni, with the spectrum dominated by oxidized nickel species. The line shape of the Ni 2p region and the Ni $2p_{3/2}$ at 855.7 eV allows the exclusion of NiO, although it does not enable a clear distinction between $Ni(OH)_2$ and NiOOH due to their very similar binding energies and spectral features. Insights on the chemical nature of the outermost layers is provided by the analysis of the Ni $L_3M_{45}M_{45}$ Auger peak, which exhibits a low kinetic energy (KE) feature at 833.2 eV characteristic of NiOOH.[21] This assignment is further supported by the calculated modified Auger parameter (BE Ni$2p_{3/2}$ + KE Ni $L_3M_{45}M_{45}$), equal to 1700.0 eV and consistent with the value for NiOOH as reported in literature.[21] In conclusion, XPS analysis of the used PTL indicates that the surface is predominantly composed of oxidized nickel species. Although the Ni 2p spectral features do not allow a clear distinction between $Ni(OH)_2$ and NiOOH, the analysis of the Auger peak and parameter provides strong evidence for the presence of NiOOH, suggesting that the passivation layer is primarily composed of NiOOH.

It is therefore proposed that during the first 24 hours of operation, the passive NiOOH layers gradually formed and reached a stable configuration, effectively modulating the electrochemical response of the electrode and limiting further corrosion.[19,22] As shown in Figure 5c, after 48 hours, the iR-corrected polarization curve exhibits lower potentials, consistent with the previously discussed break-in effect, in which the cell requires several hours of operation to reach full stabilization and activation.

4 Conclusions

In this study, the electrochemical processes of an AEM electrolyzer cell were monitored and studied separately in the full device during a 48 hour test at 1 A cm^{-2} in 1 M KOH at 50°C. The OER, HER and ion transport within the catalyst layer were fully identified using DRT analysis. The break-in effect was observed during the first hours of operation, with polarization resistances decreasing across all the electrochemical processes. The surface reconstruction of the active NiOOH phase in the anodic NiFe hydroxide catalyst was clearly tracked via galvanostatic EIS, showing a significant reduction of the low frequency semicircle associated with the OER after 24 hours. Although a cell activation procedure was performed before durability test, the anodic electrocatalyst appeared fully activated after 24 hours of operation at 5 A in this study.

Negative loops at low frequency in the Nyquist plot were attributed to corrosion phenomena leading to the formation of a passivation layer on the nickel PTL in the anodic compartment. This allowed the corrosion process of the PTL to be discerned from the other electrochemical processes occurring in the full cell set-up.

XPS analysis confirmed the formation of a NiOOH passivation layer on the PTL in the anodic compartment. While this layer did not compromise the catalytic activity and the overall polarisation performance of the MEA, an increase in ohmic resistance was measured, attributed to the passivation layer at the electrical interface between the catalyst, PTL and anode plate.

Author contributions

E.C. Conceptualization, Data curation, Formal analysis, Writing original draft; **E.S.** Methodological support, review & editing; **M.R.** Investigation, Data curation, review & editing, **C.D.** Conceptualization, Supervision, Resources, Funding acquisition, Writing – review & editing, Project administration.

Conflicts of interest

The authors declare that there are no conflicts of interest.

Data availability

The data supporting this article are available from the corresponding authors upon reasonable request.

Acknowledgements

This work was partially financed by the project PUSH2Green (RSH2A_000019, Italian Ministry of Environment and Energy Security – MASE), within the National Recovery and Resilience Plan (PNRR), Mission 2 “Green Revolution and Ecological Transition”, Component 2 “Renewable Energy, Hydrogen, Network and Sustainable Mobility”, Investment 3.5 “Hydrogen Research and Development”, European Union – NextGenerationEU. The Veneto Region is acknowledged for the Progetto LEONE (CUP B49H26000010003), granted in the framework of PR Veneto FESR 2021-2027.

The authors acknowledge Alesandro Longato and Nicola Caoduro of Pietro Fiorentini S.p.A. for their support. Pietro Fiorentini Spa is also acknowledged for supplying the electrolyzer cell and the electrodes. The ESCALAB QXi spectrometer was funded by the Italian National Research Council via the grant: “Sviluppo delle infrastrutture e programma biennale degli interventi del Consiglio Nazionale delle Ricerche (2019).”

Notes and references

1 G. Hinds and E. Brightman, *Electrochem. Commun.*, 2012, **17**, 26–29.
2 Q. Xu, S. Z. Oener, G. Lindquist, H. Jiang, C. Li and S. W. Boettcher, *ACS Energy Lett.*, 2021, **6**, 305–312.
3 S. Nuggehalli Sampathkumar, T. B. Ferriday, S. Daviran, H. Moussaoui, P. Aubin, K. Lawand, M. Mensi, P. A. Schouwink, A. Taureg, V. Subotić, A. P. L. Thévenot, F. Dionigi, P. Strasser and J. Van Herle, *Energy Fuels*, 2025, **39**, 16485–16500.
4 M. Ranz, B. Grabner, B. Schweighofer, H. Wegleiter and A. Trattner, *J. Power Sources*, 2024, **605**, 234455.
5 X. Huo, G. Shan, L. Yang, L. Gao, Y. Wang, M. Zhang, Y. Fu, W. Li and J. Zhang, *Int. J. Hydrog. Energy*, 2024, **53**, 684–697.
6 A. Valli and E. Castioni, IT202000008785A1, 2021.

View Article Online
DOI: 10.1039/D6SE00452K

7 S. Campagna Zignani, M. L. Faro, A. Carbone, C. Italiano, S. Trocino, G. Monforte and A. S. Aricò, *Electrochimica Acta*, 2022, **413**, 140078.
8 D. Li, A. R. Motz, C. Bae, C. Fujimoto, G. Yang, F.-Y. Zhang, K. E. Ayers and Y. S. Kim, *Energy Environ. Sci.*, 2021, **14**, 3393–3419.
9 I. Galkina, A. Y. Faid, W. Jiang, F. Scheepers, P. Borowski, S. Sunde, M. Shviro, W. Lehnert and A. K. Mechler, *Small*, 2024, **20**, 2311047.
10 S. Campagna Zignani, M. L. Faro, A. Carbone, C. Italiano, S. Trocino, G. Monforte and A. S. Aricò, *Electrochimica Acta*, 2022, **413**, 140078.
11 L. Armelao, M. Rando, S. Carlotto, I. Motta, G. Bottaro and M. Rancan, *Pure Appl. Chem.*, 2024, **96**, 69–80.
12 T. H. Wan, M. Saccoccio, C. Chen and F. Ciucci, *Electrochimica Acta*, 2015, **184**, 483–499.
13 M. Saccoccio, T. H. Wan, C. Chen and F. Ciucci, *Electrochimica Acta*, 2014, **147**, 470–482.
14 X. Huo, G. Shan, L. Yang, L. Abrar, L. Gao, W. Li and J. Zhang, *Int. J. Hydrog. Energy*, 2024, **91**, 693–702.
15 Y. Zhao, V. Kumtepeli, S. Ludwig and A. Jossen, *J. Power Sources*, 2022, **530**, 231250.
16 A. Ch. Lazanas and M. I. Prodromidis, *ACS Meas. Sci. Au*, 2023, **3**, 162–193.
17 H. Ma, G. Li, S. Chen, S. Zhao and X. Cheng, *Corros. Sci.*, 2002, **44**, 1177–1191.
18 *Int. J. Corros. Scale Inhib.*, DOI:10.17675/2305-6894-2020-9-4-21.
19 L.-F. Huang, M. J. Hutchison, R. J. Santucci, J. R. Scully and J. M. Rondinelli, *J. Phys. Chem. C*, 2017, **121**, 9782–9789.
20 M. Cámaras-Miguel, K. Van Daele, N. Daems and T. Breugelmans, *International Journal of Hydrogen Energy*, 2026, **224**, 154225.
21 M. C. Biesinger, L. W. M. Lau, A. R. Gerson and R. St. C. Smart, *Phys. Chem. Chem. Phys.*, 2012, **14**, 2434.
22 R. J. Smith, R. E. Hummel and J. R. Ambrose, 1987, **27**, 815–826.

View Article Online
DOI: 10.1039/D6SE00452K

Data availability

The data supporting this article are available from the corresponding authors upon reasonable request.